

In Situ Target-Less Calibration of Turbid Media

Ori Spier
Technion - IIT
orispier@yahoo.com

Tali Treibitz
University of Haifa
ttreibitz@univ.haifa.ac.il

Guy Gilboa
Technion - IIT
guy.gilboa@ee.technion.ac.il

Abstract

The color of an object imaged in a turbid medium varies with distance and medium properties, deeming color an unstable source of information. Assuming 3D scene structure has become relatively easy to estimate, the main challenge in color recovery is calibrating medium properties *in situ*, at the time of acquisition. Existing attenuation calibration methods use either color charts, external hardware, or multiple images of an object. Here we show none of these is needed for calibration. We suggest a method for estimating the medium properties (both attenuation and scattering) using only images of backscattered light from the system's light sources. This is advantageous in turbid media where the object signal is noisy, and also alleviates the need for correspondence matching, which can be difficult in high turbidity. We demonstrate the advantages of our method through simulations and in a real-life experiment at sea.

1. Introduction

Recently, there is increasing interest in the effects of participating media on optical applications [1, 2, 11, 21, 25, 26, 30]. Here, we aim to recover the inherent optical properties of a homogeneous scattering medium (attenuation and scattering) such that, given a rough 3D structure we can reconstruct color-consistent scenes, i.e., an object will have the same reconstructed color regardless of the imaging distance or water properties (Fig. 1). This is crucial in order to enable color as a reliable information source for scientific research. For example, coral reefs are endangered world-wide, and their color is an important cue for their health [27].

The estimation has to be done robustly, *in situ*, since medium properties exhibit spatio-temporal variations. Some methods achieve this using additional hardware that can be cumbersome and limiting, such as calibration targets at a fixed distance [31], or a transmissometer [7]. Others use multiple images of the same object [11, 19, 32] and require correspondence matching in a challenging medium. Here we ask ourselves: can the medium reveal its properties without any external objects or hardware? The answer

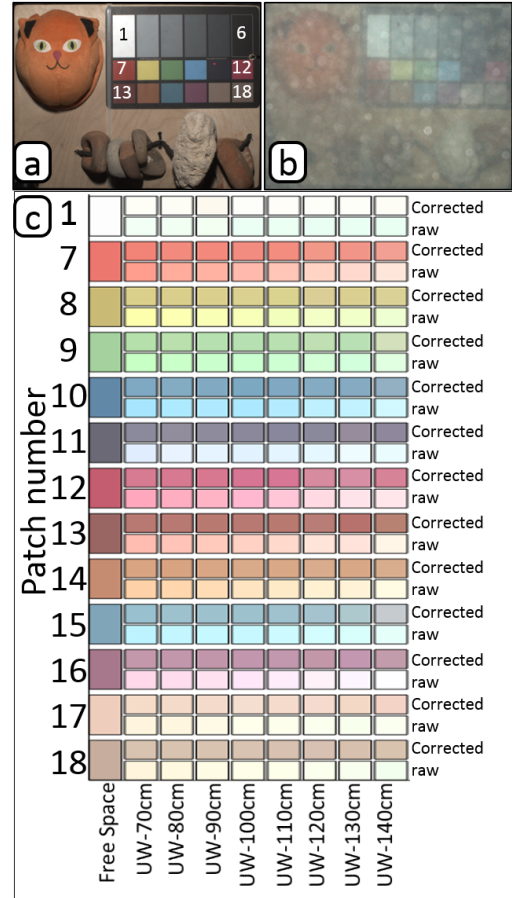


Figure 1: Color consistency visualization. a) Object imaged in free space. b) Object imaged underwater, 140cm away. c) Patches arranged in two rows per patch. Bottom rows show measured color values from underwater images along the tested distances with the free space value at the left. Color degradation is clearly visible. Top rows show the colors are significantly improved with our target-less calibration method (TL in Table. 1). Images and patches are white balanced according to free-space patch #1, and gamma corrected for presentation.

is yes. We present a novel target-less calibration method, allowing systems to almost seamlessly calibrate themselves,

while using the same hardware used for the imaging itself.

When imaging in scattering media, even when there is no object along the line-of-sight (LOS), significant signal is still acquired. This signal consists of light that is scattered back from the medium to the camera, termed *backscatter*. Most previous estimation methods are hindered by backscatter and estimate only attenuation, assuming negligible backscatter. Contrary to that, we harness the backscatter and use it as our calibration target, removing the need to carry extra hardware. We show that using two images of the backscatter in slightly varying light source locations enables estimation of attenuation. Once attenuation is estimated, it is used to estimate scattering parameters using one image. We demonstrate the advantages of our method through simulations and a real-life experiment in turbid water.

2. Previous Work

To compensate for the effects of the medium, two components need to be accounted for: attenuation and scattering. For standard color imaging, three attenuation parameters must be estimated, one per color channel. These can be accurately measured externally with a transmissometer or spectrometer [7] that are expensive and cumbersome. It is also difficult to use these measurements as-is properly in computer vision or imaging applications, due to differences in sensor spectral sensitivity and acceptance angles [8].

The most common and simple method for estimating attenuation from images is to acquire an image of a known calibration target at known distances [3, 31]. This requires a calibration target, which is also cumbersome, especially with underwater vehicles. The requirement for an external target is alleviated in several methods that use multiple images of the same object from several distances, where only their difference has to be known [32], or that are known by using a sonar [19] or structure-from-motion [11]. In [10], the grey-world assumption is used instead, but this does not always hold, for example, when looking into the water column. All these methods (except [11]) ignore backscatter. Backscatter can be ignored when the light source is put further away from the camera, but this reduces signal-to-noise-ratio [14], and sometimes difficult to implement.

Backscatter was previously removed by Tsiotsios et al. [30] by using the characteristic that backscatter saturates quickly [28], and working beyond the saturation distance. Other works removed backscatter using multiple images [28, 29]. These demonstrated visibility improvement, but not consistent physical reconstruction. The same holds for recent underwater single image methods [5, 6], and single image dehazing methods [12, 16]. In addition, until now single image methods have been demonstrated only for ambient illumination. In our case the illumination is artificial and its non-uniformity precludes their application. In [11] backscatter is estimated using a simplified model in a global

optimization framework, requiring multiple object images.

In general, fully modeling scattering requires estimating many parameters: scattering coefficient per wavelength per angle. The popular Henyey-Greenstein approximation [17] relaxes this difficult requirement by formulating a phase function that depends on two parameters per wavelength. Thus, in the case of color imaging, nine parameters are required. These have previously been estimated in a controlled lab setup [23] that imaged the appearance of a diffuse light bulb in a diluted medium. The medium parameters were found by minimizing the error of the difference between medium and clear water images vs. theoretical single scattering image formation model. To implement this method *in situ* an additional diffuse lamp that is not used for imaging needs to be added. We want to avoid that as in underwater vehicles it means requiring additional power, space, cables and hardware. In [13], the method from [23] was extended to handle any phase function, using fixed size samples in an optical table setup and comparing a Monte-Carlo simulation to 18 acquired images.

Compared to previous works, we propose a simple and efficient *in situ* method for turbid water medium parameters calibration based on *back-scattered* light, that uses only the actual hardware used for imaging. Our method is the only *in situ* method that calibrates both attenuation and scattering properties and once the calibration is done, the color can be reconstructed from single object images.

3. Image Formation Model

The setup (depicted in Fig. 2) contains a pinhole camera at world coordinates $\mathbf{X}_{\text{cam}} = (0, 0, 0)$, with the z -axis defined as the optical axis. An artificial light source is located at \mathbf{X}_S and an object at \mathbf{X}_O (Fig. 2 left). We assume ambient light can be neglected as it is significantly weaker than the artificial source, or can be acquired and subtracted. The direction of the main light source axis is \hat{d}_S (a unit vector). The total irradiance I_t sensed on the pixel \mathbf{x} is composed of two components [18, 28]:

$$I_t(\mathbf{x}) = I_d(\mathbf{x}) + B(\mathbf{x}) , \quad (1)$$

where I_d is the direct component—the attenuated object signal. The term B is the *backscatter*, that is composed of light that is scattered back from the medium into the sensor along the LOS, carrying no object information. We neglect forward scattering following [28] that showed this component is usually weaker than the other two. For clarity the coordinate notation \mathbf{x} is omitted from now on. We assume images are corrected for vignetting before processing.

In each color channel $k = R, G, B$ the object signal I_d is:

$$I_d^{(k)} = \frac{I_S^{(k)} \cdot Q(\theta) \cdot \cos(\phi) \cdot L_O^{(k)} \cdot e^{-c^{(k)} \cdot (R_S + R_{\text{cam}})}}{R_S^2} \quad (2)$$

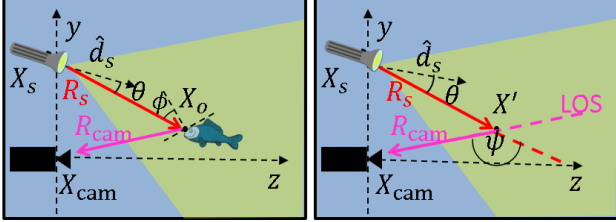


Figure 2: Image formation model and notations. [Left] Components of the signal arriving from object, I_d . [Right] Components forming a single scattering event, $B_{\text{point}}(\mathbf{X}')$. Integrating $B_{\text{point}}(\mathbf{X}')$ along the LOS yields the backscatter signal B .

where I_S is the source intensity adapted to the camera sensitivity. We assume the spatial distribution of the light source Q is radially symmetric, depending on θ , the angle between source direction and object. We assume the source illuminates not more than half a sphere, i.e., $Q(\theta > \pi/2) = 0$. L_O is the reflectance of the object. We assume the object is Lambertian, such as in [11], i.e., light is scattered from the object equally in all directions, and depends on the cosine of the angle ϕ between the incident light direction and the normal of the surface. The medium attenuates the light exponentially as a function of the attenuation coefficient c . The distances R_S and R_{cam} depict the distance between source and object, and between object and camera, respectively. In addition, the light source is subject to free space falloff $1/R_S^2$. Note that (k) indicates the color channel, and not a power operation.

For scattering, we follow the single scattering model [28], i.e., every ray emitted from the source goes through not more than one scattering event before reaching the sensor. A scattering event from a point in space \mathbf{X}' contributes:

$$B_{\text{point}}^{(k)}(\mathbf{X}') = I_S^{(k)} \cdot Q(\theta) \frac{e^{-c^{(k)} \cdot [R_S + R_{\text{cam}}]}}{R_S^2} \beta^{(k)}(\Psi), \quad (3)$$

where β is the Volume Scattering Function (VSF) of the medium, that depends on the scattering angle Ψ and color. The variables R_s , R_{cam} , Ψ depend on the coordinate \mathbf{X}' .

The total backscatter signal B stems from integrating $B_{\text{point}}^{(k)}(\mathbf{X}')$ along the LOS from the camera to the imaged object at X_O .

$$B^{(k)} = \int_0^{X_O} B_{\text{point}}^{(k)}(\mathbf{X}') d\mathbf{X}' . \quad (4)$$

When there is no object along the LOS the integration ends at infinity and we denote the resulting backscatter B_∞ ,

$$B_\infty^{(k)} = \int_0^\infty B_{\text{point}}^{(k)}(\mathbf{X}') d\mathbf{X}' . \quad (5)$$

The shape of the scattering function in the ocean (as a function of both color and angle) mostly depends on the

distribution of the sizes and types of the scattering particles in the water. Due to the complexity of measuring such data there are not many measurements available. The two main sets that are used are from [24] and [20]. All these measurements were taken by using instruments with narrow band sensitivity centered around 520nm. Extrapolations are suggested in [22].

Here, we follow a common approximation [23] and model the VSF by the Henyey-Greenstein Phase Function (HGPF) [17]:

$$\beta^{(k)}(\Psi, g) = \beta_{\text{HG}}^{(k)} \frac{1 - (g^{(k)})^2}{1 + (g^{(k)})^2 - 2g^{(k)} \cos \Psi} \quad (6)$$

where β_{HG} , g are parameters describing the medium.

The analysis above demonstrates why when objects are imaged in a medium their color varies with distance and medium properties. Combining Eqs. (1,2), the recovered object intensity is:

$$L_O^{(k)} I_S^{(k)} = \frac{\left[I_t^{(k)} - B^{(k)} \right] \cdot R_S^2 \cdot e^{c^{(k)} \cdot (R_{\text{cam}} + R_S)}}{Q(\theta) \cdot \cos(\phi)} . \quad (7)$$

Examining Eq. (7) the correction parameters can be divided into several groups. First, geometrical setup variables that can be measured: camera and source locations X_S and X_{cam} and light source direction \hat{d}_S . Second, hardware properties (Q) that can be calibrated. Third, scene structure X_O that can be roughly estimated (by stereo, sonar, etc.) [26]. Last, medium parameters ($c^{(k)}$, $g^{(k)}$, $\beta_{\text{HG}}^{(k)}$), which require calibration per color channel in every medium.

4. Medium Parameters Calibration

In this section we detail our proposed calibration algorithms. First, we combined and improved several existing methods that use object images for calibration, to use as a baseline for comparison. This method is termed Object Based (OB) from now on. Second, we describe our novel Target-Less (TL) calibration method, split into the attenuation calibration step, and scattering calibration step.

4.1. Object Based (OB) Method

To have a baseline to compare to, we have improved the method suggested by Yamashita et al. [32]. There, the attenuation coefficient c is estimated using two images of the same object acquired at different distances from the camera while assuming the backscatter is negligible. Then,

$$c = \frac{\ln \left[\frac{I_{t,1}}{I_{t,2}} \left(\frac{R_{S,1}}{R_{S,2}} \right)^2 \cdot \frac{Q_1}{Q_2} \cdot \frac{\cos(\phi_1)}{\cos(\phi_2)} \right]}{(R_{S,2} + R_{\text{cam},2} - R_{S,1} - R_{\text{cam},1})} , \quad (8)$$

where the sub-indexes 1 and 2 represent two different images. This method was originally demonstrated in a water tank, and as we show later the method is not stable as-is.

We made several improvements to make it more robust. First, [32] completely ignores backscatter. In the case of a high turbidity medium this harms the results. Therefore, as suggested in [30], before applying Eq. (8) we subtracted from the images a saturated backscatter signal B_∞ , imaged beforehand, in order to overcome the backscatter effect. This is also not enough as-is, because a single backscatter image is noisy. Therefore we extended [30] and used an average of 5 backscatter images as the backscatter signal.

Second, instead of 2 object images we used 8 images in different distances and calculated c using Eq. (8) for all $\binom{8}{2} = 28$ possible image pairs. This yielded 28 *different* estimated values for c . To choose among them we applied a voting scheme – the value that got the most votes was chosen as the calibration result (we used 0.025m^{-1} increments). This worked well in clear water. However, in turbid water the voting was not decisive and we chose the median value of all estimations as the result. Note that this method represents all object-based methods, such as [11], as they are based on the same calibration equation, with added steps for 3D estimation and registration of images.

4.2. Target-Less (TL) Calibration: Attenuation

Here we show that by using at least two backscatter images the attenuation coefficient can be derived, without using any calibration target.

Let us consider two backscatter images, B_∞^I and B_∞^{II} that are taken with two different source locations, where the source is moved Δz along the optical axis between acquisitions. The light source points forward, i.e., $\hat{d}_S = [0, 0, 1]$, and all light from source is emitted forward. Since we are looking at B_∞ images (i.e., no object along the LOS), the coordinates of this movement can be described by the camera movement, as depicted in Fig. 3a,b:

$$z_{\text{cam}}^{II} = z_{\text{cam}}^I - \Delta z, (x, y)_{\text{cam}}^I = (x, y)_{\text{cam}}^{II} = (0, 0). \quad (9)$$

For the pixel at $\mathbf{x} = 0$, i.e., the pixel whose LOS is the optical axis., the difference between each point \mathbf{X}' along the LOS in the calculation of B_∞^I and B_∞^{II} is just R_{cam} :

$$R_{\text{cam}}^{II}(\mathbf{X}') = R_{\text{cam}}^I(\mathbf{X}') + \Delta z, \forall \mathbf{X}'. \quad (10)$$

The rest of the parameters are related to the source, and therefore do not change. Plugging Eq. (10) in Eq. (5) yields the simple relation

$$B_\infty^{II}(\mathbf{x} = 0) = e^{-c \cdot \Delta z} \cdot B_\infty^I(\mathbf{x} = 0). \quad (11)$$

Then based on Eq. (11), the attenuation coefficient c per color channel k is:

$$c^{(k)} = -\frac{1}{\Delta z} \ln \frac{(B_\infty^{II})^{(k)}}{(B_\infty^I)^{(k)}}. \quad (12)$$

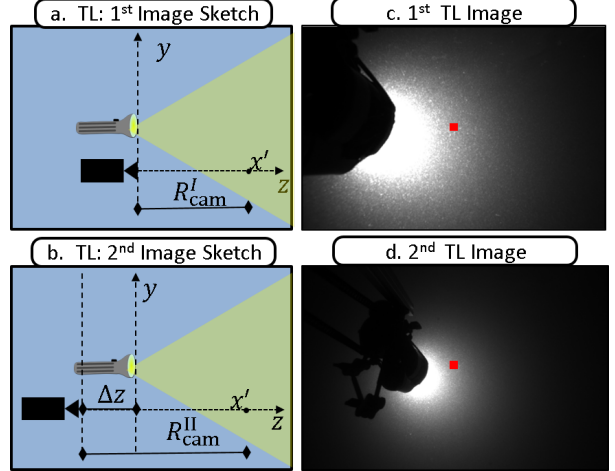


Figure 3: Image formation of the target-less attenuation estimation method. a,b) The camera images an area with no object, and then moved Δz backwards. Due to the geometrical symmetry, the difference in the B_∞ value at the central pixel between the two images, is just the attenuation in the added Δz path to the camera. c,d) Actual calibration images taken underwater (green channel), the red squares denote the central image area, from where the calibration values are taken. Black object in the left is the strobe. Image areas close to the strobe are overexposed to have enough SNR in the central area.

Since the calibration image is an image of the medium itself, there is no need for finding correspondence between multiple images of the same object as in [11, 32], which can be difficult in a turbid environment. Using $\mathbf{x} = 0$ to estimate attenuation decouples the attenuation from scattering and stabilizes the calibration.

In order to increase the robustness of this method we took the median value from a square of 100X100 pixels at the center of the frame. Furthermore, we used more than 2 images, performing a least squares linear fit between log of the intensity and source offset. The negative slope of this linear fit is the attenuation coefficient c . To handle outliers we try all fits that have up to 25% outliers and choose the one with the lowest RMS error. The linear fit quality can be used as an indication for the accuracy of the calibration, a criterion that is missing in other methods.

The backscatter at the center of the image has to be strong enough for the camera to sense. This means that the method is less suitable for clear water. In our experience, the method worked well with our setup in approximated daylight visibility of 1m to 6m (i.e., the approximated distance at which a diver recognizes his buddy underwater).

Fig. 4 depicts simulated properties and expected performance of this method according to the single scattering model. Fig. 4a demonstrates a single calibration with and without noise. Noise was modeled as photon noise model with an STD of 1% from signal intensity, which yields a 3%

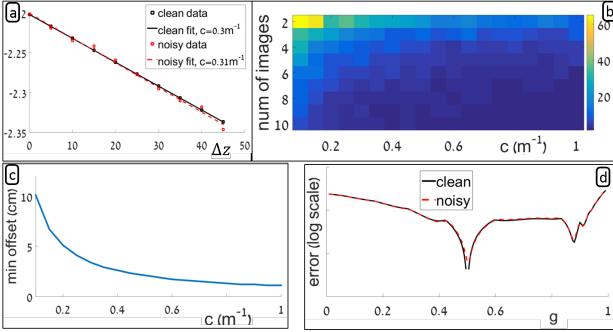


Figure 4: TL simulations. a) Clean and noisy simulation of TL, showing log of central image intensity vs. source offset ($c = 0.3\text{m}^{-1}$, $g = 0.55$), using 1% photon noise. b) Average relative error vs. number of calibration images and c value, with 1% photonic noise. For each case, 500 simulations of attenuation extraction were performed. As the turbidity *increases*, less images are needed. c) Minimal source offset required in order to achieve 1% intensity difference at center of image. The higher the attenuation, the smaller this distance can be. Even in low attenuation less than 10cm are needed. d) g Calibration. After estimating attenuation, the method in Sec. 4.3 yields the expected value ($g = 0.5$) in both clean and 1% photonic noisy cases.

error. Fig. 4b depicts the dependency of the accuracy on the number of images used (each one is taken at a different offset), and c . More images or a higher turbidity yield a smaller error. However, the marginal contribution of each additional image decreases. The advantage of our method is that as the turbidity *increases*, less images are needed. This is in contrast to object-based methods that suffer loss of SNR in higher turbidity. Fig. 4c depicts the minimal source offset needed in order to get a 1% difference in central pixel intensity between two images, as a function of c . The higher the attenuation, the smaller offset is needed, but even in low attenuation less than 10cm are needed, which makes the method very feasible to implement, e.g., by mounting two strobes in slightly different positions.

4.3. Target-Less Calibration: Scattering

Once c is calibrated, one calibration image can be used in order to estimate the scattering parameters.

Plugging Eq. (6) into Eq. (5) yields

$$B_\infty = G \int_0^\infty Q \frac{e^{-c \cdot (R_S + R_{\text{cam}})} \cdot (1 - g)}{R_S^2 \cdot (1 + g^2 - 2g \cos \Psi)} d\mathbf{X}', \quad (13)$$

where the gain G is defined as $G = I_S \beta_{HG}$.

Examining Eq. (13), we see there are two unknown medium parameters left after c is estimated: G , and g . We propose to solve them by the following optimization:

$$(\tilde{g}, \tilde{G}) = \min_{g \in \Omega_g} \min_{G \in \Omega_G} [E(B_\infty^{\text{measured}}, B_\infty^{\text{simulated}})], \quad (14)$$

where E is an error measure, Ω_G the range of possible gain values and $\Omega_g = (0, \dots, 1)$. This is done separately for each color channel. Theoretically, c could have been solved for in the same optimization but our simulations and experiments have shown that when c is unknown Eq. (14) does not have a single global minimum (detailed in the supplementary material).

To speed the minimization of Eq. (14) and make it more robust to noise we propose to use a symmetric B_∞ image and exploit the symmetry. For example, the backscatter image in Fig. 7a was taken with the source located at $X = 0$, pointing parallel to the optical axis, such that the resulting backscatter image is symmetric along the y axis.

We construct a vector from the values along the symmetry axis of B_∞ (Fig. 7a) and solve Eq. (14) along it. We term it the *backscatter center-line*. For each value of $g \in \Omega_g$, we find the best fit $G \in \Omega_G$ in the L_2 sense. The final solution is the pair of g and G that yield the lowest error. A simulation of the error as a function of g is shown in Fig. 4d. The minimum in both the clear and noisy image is the ground truth value in the simulation $g = 0.5$.

5. Real-World Experiments

5.1. Experimental Setup

We performed our experiments in real conditions at sea by scuba-diving. We used a Nikon D810 SLR camera, capable of acquiring raw linear images, with a 20mm Nikon lens. It was housed in a Hugyfot housing with a dome port. We used Inon Z240 underwater strobes. The experimental frame was custom built using aluminum rails (Fig. 5). We used an underwater color-chart (DGK Color Tools) as our target object, attached to the rail so it can move along the optical axis, and stay perpendicular to it, at distances of 70 – 140cm. For TL (Sec. 4.2), the light source was placed on a rail to the side of the camera, that can move horizontally in parallel to the optical axis (Fig. 5c) and was moved in 5cm steps. Tick marks were drawn on the rail to enable control on the source distance. Saturated backscatter images were taken by pointing the setup to an area without any object. We set the focus and depth-of-field such that the entire significant backscatter is inside the depth-of-field for all distances. For the scattering calibration the source was attached to the camera housing using an off-the-shelf ball attachment. Note that we used standard off-the-shelf Xenon strobes that are known to have up to 5% fluctuations in intensity [28] and this method relies on having a stable source. To minimize this effect we waited several seconds between acquisition to make sure the strobe is fully recharged.

5.2. System Pre-Calibrations

Our method requires some pre-calibrations, preferably done underwater. Vignetting was calibrated in daylight by placing the camera on a tripod and capturing images

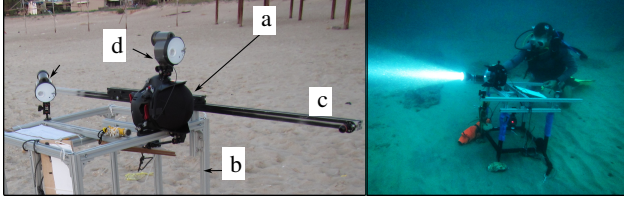


Figure 5: Conducting real-life experiments. [Left] Our setup. An SLR camera housed in an underwater housing (a) is mounted on an aluminum frame (b). A rail (c) that can move parallel to the optical axis is attached to it. The strobe (d) and object are later mounted on the rail for controlled-distance experiments. [Right] An underwater view of our system. Light cone is clearly visible, we use it for estimating water properties.

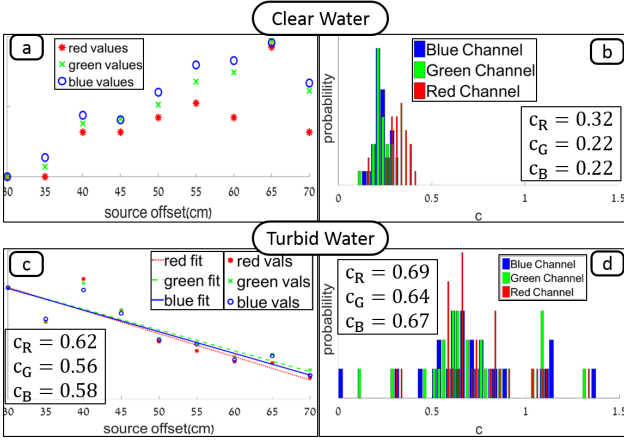


Figure 6: Attenuation estimation. Experimental results using both methods in clear [top row] and turbid [bottom Row] sea water experiments. OB [right Column], as expected, gives a stable result in clear water (narrow histogram), but loses stability in turbid water (OB was calculated using the white patch). TL [Left Column] fails in clear water, however behaves as expected in turbid water (good linear fit). All values are in m^{-1} units.

of a white static calibration patch while rotating the camera between images. This calibration was not done underwater since we did not have a stable underwater light source. Camera intrinsic parameters were calibrated underwater with a checkerboard and using the camera calibration toolbox [9]. Source angular distribution Q was calibrated in a water tank. We used a static camera pointing at a calibration target, while rotating the source. We rotated the source both around its primary axis (\hat{d}_s), and its perpendicular direction (which modifies θ_s). As expected, results showed radial symmetry around the primary axis, and a cosine distribution around its perpendicular direction.

5.3. Attenuation Calibration Results

We present results from two experiments (Fig. 6), conducted at sea in clear water (CW) and turbid water (TW). We compare the performance of TL and OB under these

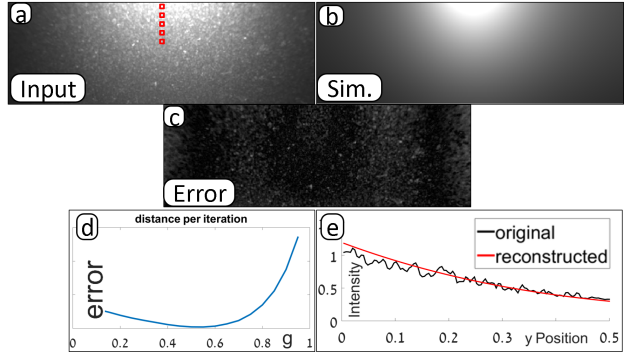


Figure 7: Estimating scattering properties (g) of red channel, in TW. a) Backscatter calibration image (B_∞) acquired *in situ*. Note the in-homogeneous medium. b) Rendered B_∞ using the calibrated attenuation and scattering parameters. c) Relative difference image between the rendering and the input image (linear display). d) The error of Eq. 14 as a function of g . The minimum is at $g=0.55$. e) Values at the backscatter center-line, calibration and reconstruction values.

different conditions.

Fig. 6a,b depict the result of applying both methods in clear sea water. OB works well (the histogram is narrow), whereas TL fails due to weak backscatter values that results in a low SNR. In TW (Fig. 6c,d) we see the results of OB are spread and it fails to produce a reliable result, whereas TL behaves as expected, and produces a reliable linear fit, with acceptable outliers.

Results of attenuation calibration in the TW experiment are: $c_R = 0.62m^{-1}$, $c_G = 0.56m^{-1}$, $c_B = 0.58m^{-1}$ using TL and $c_R = 0.69m^{-1}$, $c_G = 0.64m^{-1}$, $c_B = 0.67m^{-1}$ in OB. As expected, red channel attenuation is stronger than the green and blue channels. Additional TL attenuation calibration results are shown in the supplementary material.

5.4. Scattering Calibration Results (g, G)

Implementation details: We sampled $m = 26$ points along the backscatter center line, along the top 30% of this axis in the image, taking the median value of all pixels from a 100×100 square centered around each point. The reason for using only the top part of the image is that on the top part the signal is stronger, therefore less subject to noise.

Scattering calibration in TW was done by using the same backscatter images used for OB. Fig. 7 shows the measured signal (average of 5 images taken), next to the rendered backscatter image resulting from the calibrated parameters, along with an image showing the relative difference between the two. Numeric results: $g_R = 0.55$, $G_R = 0.2$, $G_G = 0.55$, $G_B = 0.45$, $G_B = 0.39$.

5.5. Evaluation Using Color Consistency

Since we do not have ground truth of water properties, we judge the results by quantifying color consistency. This

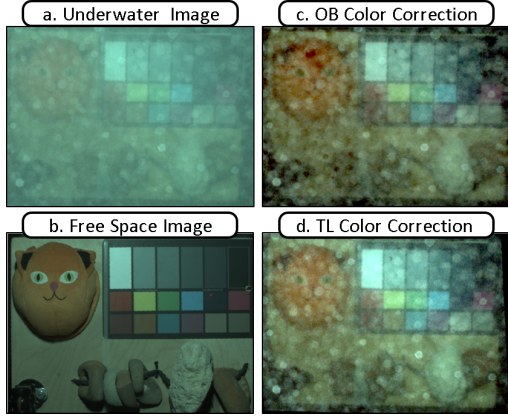


Figure 8: Object reconstruction results. (a) Object image taken underwater at a distance of 140cm from camera. (b) Object image in free space. (c) Color corrected image of the underwater object using object based (OB) Method. (d) Color corrected image using target-less (TL) method. Images are gamma-corrected for display purposes. Notice we did not apply any denoising.

means that if the estimated properties are correct, the colors of an object at various distances can all be corrected to the same value using Eq. (7) regardless of the imaging distance in the medium, and, they should be consistent with a free-space image of the same object taken with the same setup. This is also one of the important applications for our method: recovering color-consistent underwater images that can be used for scientific applications.

We acquired underwater images of a target object in different distances from the camera. Fig. 8 demonstrates the degradation of an object between free-space (b) and an underwater distance of 140cm (a), and our corrections (c,d).

For quantitative evaluation, we compare the colors in linear RGB space. Each color can be viewed as a vector in RGB space. We define the distance between two colors A_1 and A_2 as the angle α between these vectors:

$$\cos \alpha = A_1 \cdot A_2 / (|A_1| \cdot |A_2|) . \quad (15)$$

This measure ignores global image intensity which we do not aim to recover.

We compare results from several methods (summarized in Table 1). All consist of two basic steps: backscatter removal, and attenuation compensation. Backscatter can be removed by two methods. In the first (used in TL:sat, OB) we subtract saturated backscatter following [30], where we use an average of 5 backscatter images to reduce noise. In the second (used in TL) we calculate B using the known geometry and parameters by TL (c, g and G). Attenuation is compensated using Eq. (7) with calibrated c either by TL or OB. We also demonstrate the effect of correcting only a single degradation factor in TL (TL:a, TL:b).

Table 2 depicts a quantitative comparison of the error (α)

name	backscatter removal	attenuation correction
TL:a	none	TL result (c)
TL:b	TL result (g, G)	no
TL	TL result (g, G)	TL result (c)
TL:sat	saturated image subtraction	TL result (c)
OB	saturated image subtraction	OB result

Table 1: Summary of tested methods. Notice the first two (TL:a, TL:b) are shown to demonstrate the effect of correcting only a single degradation factor in TL.

patch	raw	TL:a	TL:b	TL	TL:sat	OB
1	2.9	1.5	3.6	1.8	1.9	1.8
2	2.6	1.3	3.5	1.7	2.3	2.1
3	2.8	1	3.5	1.6	1.8	2.3
4	2.7	0.8	3.6	1.8	1.9	2.5
5	2.1	0.9	3.9	3.7	3.9	4.3
6	2.8	1.2	5	5.5	10.1	9.4
7	21.1	18.1	12.9	9.1	6.5	7.6
8	9.9	9.9	5.3	4	3.1	3.5
9	5.3	7.7	1.8	4.6	4	3.4
10	8.3	8.2	5.8	5.0	4.5	4.2
11	3.9	2.3	2.7	1.9	4.3	4.5
12	20.1	16.9	14.2	11.0	9.1	10.0
13	11.0	7.9	6.3	5.3	10.4	9.4
14	12.0	9.7	7.4	3.7	3.7	4.3
15	6.4	7.0	6.2	6.4	6.5	6.0
16	9.3	6.2	6.4	3.1	2.2	2.9
17	5.1	3.2	3.9	1.6	1.5	1.8
18	5.4	3.4	4.6	1.5	3.7	3.2
median	8.3	7.7	5.8	4	4	4.2

Table 2: A quantitative comparison of the error (α) between the free space image and correction of the furthest image (worst color deterioration), from the TW experiment. Methods are detailed in Table 1. Median was calculated excluding patches #2 ... #6 as they have the same color as #1.

between the free space image and correction of the furthest image (worst color deterioration). We compare five different variants that differ in the backscatter removal method and attenuation compensation (summarized in Table 1). The analysis is conducted on all patches of the color-target. Patches are numbered from left to right between 1 – 18, where 1 stands for the top-left white patch, 6 stands for the top right black patch, and so on (see Fig. 1).

The colors are visualized in Fig. 1, that depicts the colors of the raw patches in all distances together with our correction. The deterioration of raw color with distance is clearly visible, and so is the effectiveness of our correction.

Fig. 9 depicts in more detail the color consistency results of four selected patches in different colors (white, red, yellow, and brown) along all tested distances. Graphs for all patches are found in the supplementary material.

Looking at the median values, the attenuation coeffi-

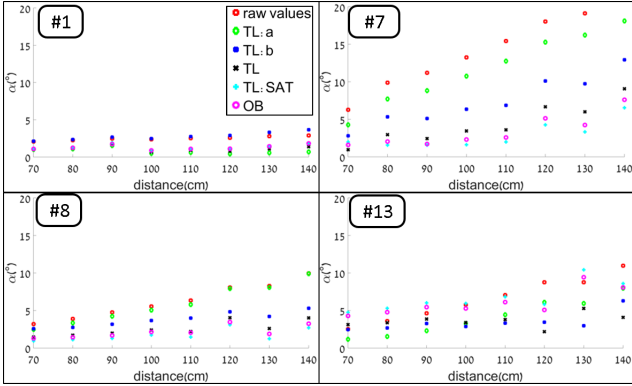


Figure 9: Color consistency results of four patches. A comparison of correction methods for patches #1,7,8,13, in different underwater distances. Different colors degrade differently, and both TL and OB methods improve color consistency. Similar graphs for all color patches are shown in the supplementary material.

lients from TL perform slightly better than OB. Note that OB was implemented in favorable conditions, where the registration between images was done manually. In practice, doing it automatically can be difficult. For backscatter removal, Using g (TL) or saturated backscatter (TL:sat) show similar median performance, but the performance is not consistent and changes significantly between patches. In some TL achieves half the error of TL:sat and in some the opposite. This is probably due to real-environment outliers such as particles in both the calibration and observed images. TL:sat is faster to implement, however using g may add an insight on the medium itself, and might be more accurate in very close distances that we did not examine.

Overall, TL, TL:sat and OB exhibit comparable performance, and all three methods significantly improve the color consistency. The differences between them might reflect limits of *in situ* reconstruction accuracy that is possible to achieve with a single attenuation coefficient per color channel (explained in Sec. 5.6). The raw error varies significantly between the patches, up to 10-fold. The color of the backscatter is close to white, so it seems the gray-levels patches barely change their color. However, their apparent color stems from the backscatter, not from reflected color. Patches that have a relatively high red value have a high raw error, and there our method has the highest influence.

5.6. Dependency of OB on Patch Color

During our experiments we noticed that the calibrated values using OB differ when the method (Eq. 8) is applied on different patches, even in the clear water experiment. This is an interesting point worth discussing although OB is not the main focus of the paper. Differences of calibrated c from several patches are depicted in Fig. 10, together with the reconstruction errors that stem from them. This hap-

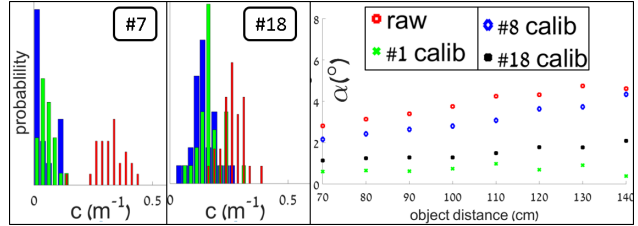


Figure 10: Clear water accuracy estimation. [left, center] attenuation calibration using OB method on two different patches (#7, #18) result in different attenuation values. [right] color consistency analysis of the white patch (#1) using these different parameters give different results. Best result is achieved when calibration is done on the object of interest itself, but this requires re-calibration for every object.

pens because different reflectances interact differently with the wavelength-dependent attenuation. This analysis suggests limits to reconstruction when using a global value for c , which we intend to explore in future work.

6. Discussion

Underwater color correction is not an easy task. Although the equations are relatively simple, many parameters and coefficients require *in situ* calibration. In addition, the medium is not completely homogeneous and is difficult to work in. Here we present two variants of a self-contained method that uses only backscatter images taken in the medium for calibration, with the same off-the-shelf components that are used for the imaging itself, without requiring external color-charts or hardware. Since it does not depend on external objects, it relieves the need for registering calibration images or object matching, which can be difficult in bad visibility conditions. This makes the hardware and implementation of our method simpler. In addition, we showed that even though we relieve the external hardware requirement, our method's performance in these difficult conditions is similar or better to using a color-chart. This was demonstrated in real, challenging conditions at sea.

From our experiments, in low-turbidity the SNR in the backscatter images is sometimes too low. Thus our method will be less stable in these cases. However, in low turbidity our method is also less needed. As we showed, it has clear advantages in high-turbidity cases as it utilizes the turbidity itself and does not regard it as an obstacle. We also suggest a quality criterion that previous methods do not have.

Our method can be applied in real-time and the setup can be especially useful in autonomous vehicles such as cars and boats imaging dynamic scenes in low visibility conditions (fog, sand-storms, etc.), and forward-looking setups underwater [4]. In addition it can provide dynamic estimation of visibility limits in autonomous systems, for example, autonomous decision on maximum safe driving speed in bad weather [15]. Future improvements may in-

clude handling ambient light, and object dependent color correction [2]. This work can lead to insights about recovery of scenes from single scene-images, i.e., requiring no calibration frames at all.

Acknowledgements

TT was supported by the The Leona M. and Harry B. Helmsley Charitable Trust and The Maurice Hatter Foundation, Ministry of Science, Technology and Space grant #3-12487. GG acknowledges support to the Israel Science Foundation (grant 718/15). Additional support was provided by the Technion Ollendorff Minerva Center for Vision and Image Sciences.

References

- [1] R. Z. A. Schwartzman, M. Alterman and Y. Y. Schechner. Turbulence-induced 2d correlated image distortion. In *Proc. IEEE CVPR*, 2017.
- [2] D. Akkaynak, T. Treibitz, T. Shlesinger, R. Tamir, Y. Loya, and D. Iluz. What is the space of attenuation coefficients in underwater computer vision? In *Proc. IEEE CVPR*, 2017.
- [3] D. Akkaynak, T. Treibitz, B. Xiao, U. A. Gürkan, J. J. Allen, U. Demirci, and R. T. Hanlon. Use of commercial off-the-shelf digital cameras for scientific data acquisition and scene-specific color calibration. *JOSA A*, 31(2):312–321, 2014.
- [4] J. Albiez, S. Joyeux, C. Gaudig, J. Hilljegerdes, S. Kroffke, C. Schoo, S. Arnold, G. Mimoso, P. Alcantara, R. Saback, et al. Flatfish—a compact subsea-resident inspection auv. In *Proc. MTS/IEEE OCEANS*, 2015.
- [5] C. Ancuti, C. O. Ancuti, T. Haber, and P. Bekaert. Enhancing underwater images and videos by fusion. In *Proc. IEEE CVPR*, pages 81–88, 2012.
- [6] G. Biancoa, M. Muzzupappa, F. Bruno, R. Garciaib, and L. Neumann. A new color correction method for underwater imaging. *ISPRS-Int. Archives Photogrammetry, Remote Sensing and Spatial Information Sciences*, 1:25–32, 2015.
- [7] D. L. Bongiorno, M. Bryson, and S. B. Williams. Dynamic spectral-based underwater colour correction. In *Proc. MTS/IEEE OCEANS*, 2013.
- [8] E. Boss, W. H. Slade, M. Behrenfeld, and G. Dall’Olmo. Acceptance angle effects on the beam attenuation in the ocean. *Optics Express*, 17(3):1535–1550, 2009.
- [9] J.-Y. Bouguet. Camera calibration toolbox for matlab. 2004.
- [10] M. Bryson, M. Johnson-Roberson, O. Pizarro, and S. B. Williams. Colour-consistent structure-from-motion models using underwater imagery. In *Robotics: Science and Systems*, 2012.
- [11] M. Bryson, M. Johnson-Roberson, O. Pizarro, and S. B. Williams. True color correction of autonomous underwater vehicle imagery. *J. of Field Robotics*, 2015.
- [12] R. Fattal. Dehazing using color-lines. *ACM Trans. Graph.*, 34(1):13, 2014.
- [13] I. Gkioulekas, S. Zhao, K. Bala, T. Zickler, and A. Levin. Inverse volume rendering with material dictionaries. *ACM TOG*, 32(6):162, 2013.
- [14] M. Gupta, S. G. Narasimhan, and Y. Y. Schechner. On controlling light transport in poor visibility environments. In *Proc. IEEE CVPR*, 2008.
- [15] N. Hautière, J.-P. Tarel, and D. Aubert. Towards fog-free in-vehicle vision systems through contrast restoration. In *Proc. IEEE CVPR*, 2007.
- [16] K. He, J. Sun, and X. Tang. Single image haze removal using dark channel prior. In *Proc. IEEE CVPR*, 2009.
- [17] L. G. Henyey and J. L. Greenstein. Diffuse radiation in the galaxy. *The Astrophysical Journal*, 93:70–83, 1941.
- [18] J. S. Jaffe. Computer modeling and the design of optimal underwater imaging systems. *IEEE J. Oceanic Eng.*, 15(2):101–111, 1990.
- [19] J. W. Kaeli, H. Singh, C. Murphy, and C. Kunz. Improving color correction for underwater image surveys. In *Proc. IEEE/MTS Oceans*, pages 805–810, 2011.
- [20] M. E. Lee, V. I. Haltrin, E. B. Shybanov, and A. D. Weidemann. Light scattering phase functions of turbid coastal waters measured in leo-15 experiment in 2000. In *Proc. IEEE/MTS Oceans*, volume 5, pages P2835–P2841, 2003.
- [21] F. L. Lobo, M. Costa, S. Phillips, E. Young, and C. McGregor. Light backscattering in turbid freshwater: a laboratory investigation. *J. of Applied Remote Sensing*, 8(1):83611–83611, 2014.
- [22] C. D. Mobley. *Light and water: radiative transfer in natural waters*. Academic press, 1994.
- [23] S. G. Narasimhan, M. Gupta, C. Donner, R. Ramamoorthi, S. K. Nayar, and H. W. Jensen. Acquiring scattering properties of participating media by dilution. *ACM Transactions on Graphics (TOG)*, 25(3):1003–1012, 2006.
- [24] T. J. Petzold. Volume scattering functions for selected ocean waters. Technical report, DTIC Document, 1972.
- [25] A. L. Y. Y. Schechner and A. B. Davis. Multiple-scattering microphysics tomography. In *Proc. IEEE CVPR*, 2017.
- [26] M. Sheinin and Y. Y. Schechner. The next best underwater view. In *Proc. IEEE CVPR*, 2016.
- [27] A. Strong, C. Barrientos, C. Duda, and J. Sapper. Improved satellite techniques for monitoring coral reef bleaching. In *Proc. Int Coral Reef Symp*, volume 2, pages 1495–1498, 1997.
- [28] T. Treibitz and Y. Y. Schechner. Active polarization descattering. *IEEE Trans. PAMI*, 31(3):385–399, 2009.
- [29] T. Treibitz and Y. Y. Schechner. Turbid scene enhancement using multi-directional illumination fusion. *IEEE Trans. Image Processing*, 21(11):4662–4667, 2012.
- [30] C. Tsotsios, M. E. Angelopoulou, T.-K. Kim, and A. J. Davison. Backscatter compensated photometric stereo with 3 sources. In *Proc. IEEE CVPR*, pages 2259–2266, 2014.
- [31] G. Winters, R. Holzman, A. Blekhman, S. Beer, and Y. Loya. Photographic assessment of coral chlorophyll contents: implications for ecophysiological studies and coral monitoring. *J. Exp. Marine Biology and Ecology*, 380(1):25–35, 2009.
- [32] A. Yamashita, M. Fujii, and T. Kaneko. Color registration of underwater images for underwater sensing with consideration of light attenuation. In *IEEE Conf. Robotics and Automation*, pages 4570–4575, 2007.